Tectonophysics 492 (2010) 213–229

Contents lists available at ScienceDirect

Tectonophysics

journal homepage: www.elsevier.com/locate/tecto

Focal mechanisms of micro-earthquakes in the Dobrá Voda seismoactive area in the Malé Karpaty Mts. (Little Carpathians), Slovakia

Lucia Fojtíková [a,b,*], Václav Vavryčuk [c], Andrej Cipciar [a], Ján Madarás [a,d]

[a] Geophysical Institute, Slovak Academy of Sciences, Dúbravská cesta 9, 845 28 Bratislava, Slovakia
[b] Faculty of Mathematics, Physics and Informatics, Comenius University, Mlynská dolina F1, 842 48 Bratislava, Slovakia
[c] Institute of Geophysics, Academy of Sciences, Boční II/1401, 141 00 Praha, Czech Republic
[d] State Geological Institute of Dionýz Štúr, Mlynská dolina 1, 817 04 Bratislava, Slovakia

ARTICLE INFO

Article history:
Received 13 July 2009
Received in revised form 13 June 2010
Accepted 17 June 2010
Available online 25 June 2010

Keywords:
Earthquake
Focal mechanism
Moment tensor
Tectonic stress

ABSTRACT

We have analyzed 44 micro-earthquakes with magnitudes between 1.2 and 3.4, which occurred in the Dobrá Voda area, Slovakia, in the period 2001–2009. The epicentres of the micro-earthquakes form a cluster elongated in the ENE–WSW direction. This direction coincides with the orientation of the main fault systems in the area: Dobrá Voda and Brezová faults. The depths of the hypocentres vary from 1 km to 14 km. Three different methods were used to calculate the focal mechanisms: (a) a method using the polarities of Pg and Pn waves, (b) the P-wave amplitude inversion of moment tensors, and (c) the waveform inversion of moment tensors. The majority of the analyzed micro-earthquakes have a left-lateral strike-slip focal mechanism with weak normal or reverse components. The full moment tensors comprise significant non-double-couple (non-DC) components. The non-DC components are partly numerical errors of the inversion but might be also of a physical origin. The most accurate values of the non-DC components are obtained from the P-wave amplitude inversion. For this inversion, the isotropic component (ISO) and the compensated linear vector dipole component (CLVD) are mostly positive and well correlated. This might indicate tensile faulting. Adopting the model of tensile faulting, we estimated the mean ratio of P to S wave velocities in the focal area from the values of ISO and CLVD, $v_P/v_S = 1.5$–1.6. The three different datasets of the focal mechanisms have been inverted for the present-day tectonic stress in the Dobrá Voda area. The slip shear stress component criterion was applied in the stress inversion. The results of the three inversions are well-consistent and point to a high reliability and good accuracy of the inverted stress. The orientations of the principal stresses are (azimuth/plunge): $\sigma_1 = 210$–$220°/5$–$25°$, $\sigma_2 = 70$–$105°/55$–$75°$, and $\sigma_3 = 305$–$315°/15$–$25°$, and the shape ratio is $R = 0.45$–0.60. The azimuth is measured clockwise from the north and the plunge downwards from the horizontal plane. The retrieved maximum compression lies along the belt of the Malé Karpaty Mts. The local tectonic stress reflects complex tectonic conditions in the area. The presence of tensile faulting might point to an extensional stress regime in the area.

1. Introduction

The Dobrá Voda area is one of the most seismically active zones on the territory of Slovakia (see Fig. 1). It is situated in the transition zone between the Eastern Alps and the Western Carpathians (Šefara et al., 1998; Lenhardt et al., 2007), specifically, at the northern margin of the Malé Karpaty Mts., between the Pieniny Klippen Belt (PKB) in the west and the Danube Basin in the east (see Fig. 2). On the surface, the PKB reflects the principal boundary between the stable European Platform and the Western Carpathians structures. The Danube Basin is characterized by thick Neogene to Quaternary sediments deposited on a thinned crust (the Moho depth is between 26 and 30 km). The dominant brittle structures of the Dobrá Voda area are ENE–WSW trending fault zones (see Fig. 2). The Brezová fault zone forms the northern margin of the Brezová elevation, while its southern border with the Dobrá Voda depression is represented by the distinctive Dobrá Voda fault zone (e.g. Marko et al., 1991).

In the last century, the strongest earthquake occurred in the Dobrá Voda area on January 9, 1906 (see Fig. 2) with a magnitude of 5.7 and was followed by an aftershock of magnitude 5.1 on January 19, 1906 (Réthly, 1907; Kárník, 1968; Zsíros, 2005). In 1904, 1930 and 1967, other earthquakes with magnitudes between 4.0 and 5.0 were observed. The seismic activity is instrumentally monitored by the local seismic network MKNET, installed in this area in 1985, and additionally by the Slovak National Seismic Network (Cipciar et al., 2002). The seismic activity is monitored also by the micro-displacement monitoring network (Briestenský et al., 2007). The

* Corresponding author.
E-mail address: geoflufo@savba.sk (L. Fojtíková).

0040-1951/$ – see front matter © 2010 Elsevier B.V. All rights reserved.
doi:10.1016/j.tecto.2010.06.007

strongest earthquake recorded by network MKNET occurred on March 13, 2006 with a magnitude of 3.4.

In this paper, we study the double-couple focal mechanisms and full moment tensors of selected earthquakes that occurred in the Dobrá Voda area in the period 2001–2009. As input data we use Pg, Pn and local P-wave polarities, local P-wave amplitudes or complete waveforms observed at local stations. Using different input seismic data and applying different approaches, we try to estimate the accuracy and reliability of the retrieved focal mechanisms. We decompose the moment tensors into the double-couple (DC) and non-double-couple (non-DC) components in order to get more detailed information on the fracture process and on the local properties of the medium in the focal area (Frohlich, 1994; Julian et al., 1998; Miller et al., 1998; Vavryčuk, 2001, 2005; Vavryčuk et al., 2008). Finally, we invert the obtained focal mechanisms for the present-day tectonic stress in the region. Knowledge of the tectonic stress is crucial for further tectonic interpretations because existing studies on stress in the region are contradicting.

2. Data

2.1. Seismic observations

The seismic activity in the Dobrá Voda area is monitored by the Malé Karpaty seismic network (MKNET). The MKNET is a local network (see Fig. 1) which consists of 11 three-component seismic stations equipped with short-period SM-3, Lennartz Le3D or Guralp CMG-40T-1 seismometers. The corner frequency depends on the type of the seismometer installed at each station and ranges from 0.65 Hz (SM-3) to 1 Hz (Le3D, CMG-40T-1). The sampling frequency is 100 Hz. For some of events, data from other adjacent local networks and from regional short-period and broad-band stations were also available.

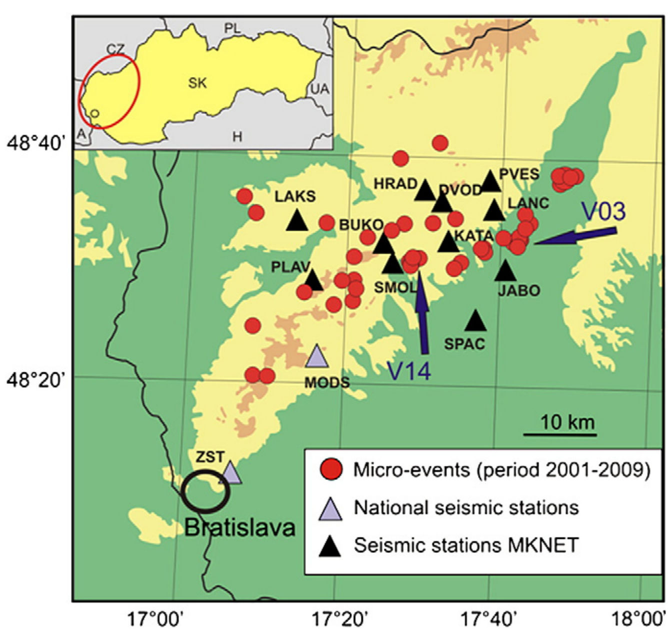

Fig. 1. Map of stations and epicentres of earthquakes. The red full circles show epicentres of the earthquakes under study. The full black and grey triangles mark the positions of the stations of the local seismic network MKNET and the Slovak National Seismic Network, respectively. The full line shows the border between Slovakia, Austria and the Czech Republic. The positions of two strongest earthquakes V03 and V14 with magnitudes of 3.4 and 3.0, respectively, are marked by arrows.

We have processed 44 micro-earthquakes with magnitudes between 1.2 and 3.4 that occurred in the period 2001–2009 (see Fig. 1 and Table 1). The Seisbase code developed for an interactive data inspection was used as the basic tool for visualizing and analyzing the local seismic data (Fischer and Hampl, 1997). The regional broad-band data were analyzed by the Seismic Handler code (Stammler, 1993). The velocity records were integrated to the displacement records to simplify the analyzed waveforms and to filter out high-frequency waves reflecting mostly local structural inhomogeneities (see Figs. 3 and 4). The records were further pre-processed by frequency filtering. The parameters of the filtering depended on the inversion method used to calculate the focal mechanisms and moment tensors. For measuring the P-wave polarities and the P-wave amplitudes, a high-pass filter with a corner frequency of 1 Hz was applied to remove low-frequency noise. In the waveform inversion, a band-pass filter with corner frequencies of 0.8 Hz and 1.6 Hz was used to extract the low-frequency content of the S waves and surface waves.

2.2. Locations

The locations of micro-earthquakes were calculated using the Fasthypo code (Herrmann, 1979). In the location procedure, we used the arrival times of P and S waves observed at local seismic stations. The structure was approximated by a 1-D layered velocity model (see Table 2). The v_P/v_S ratio was fixed and equal to 1.75. Stations for which the subsurface structure significantly deviated from the average velocity model were excluded. This concerned namely stations installed on the sedimentary rocks of the Danube Basin (stations JABO and SPAC).

The epicentres of micro-earthquakes are scattered over an area 50 km EW by 30 km NS in size (see Fig. 1) and form a cluster elongated in the ENE–WSW direction. This direction roughly coincides with the orientation of the main fault systems in the area: the Dobrá Voda and Brezová faults (see Fig. 2). The depths of the hypocentres are the less accurate location parameter and vary from 1 km to 14 km. If the v_P/v_S ratio is increased to 1.80, the depth decreases by about several hundred metres to 1.5 km. Independently of the v_P/v_S ratio, the cluster of hypocentres is dipping in the EWE direction. A rather large scatter of epicentres over the whole area indicates that several faults were probably activated.

3. Focal mechanisms and moment tensors

Focal mechanisms and full moment tensors of selected events were calculated using three different inversion methods: (1) the inversion from polarities of Pg, Pn and local P waves, (2) the amplitude inversion from the vertical components of local P waves, and (3) the waveform inversion from the complete three-component seismograms observed at local seismic stations. The inversion from polarities utilizes information from local as well as regional P waves. It requires a good station coverage but it is insensitive to calibration of stations. The amplitude inversion utilizes mainly high-frequency local P waves and requires well-calibrated stations. The waveform inversion is based on the inversion of the low-frequency content of the S waves and local surface waves. This method requires high-quality data and accurate knowledge of the crustal model.

Since the three inversions utilize different frequency bands, different types of waves and different methods of calculating the Green functions, the inversions can be considered as independent. Hence, a comparison of the focal mechanisms and moment tensors produced by the three methods allows us to estimate the reliability of the results and the efficiency and accuracy of the inversion methods.

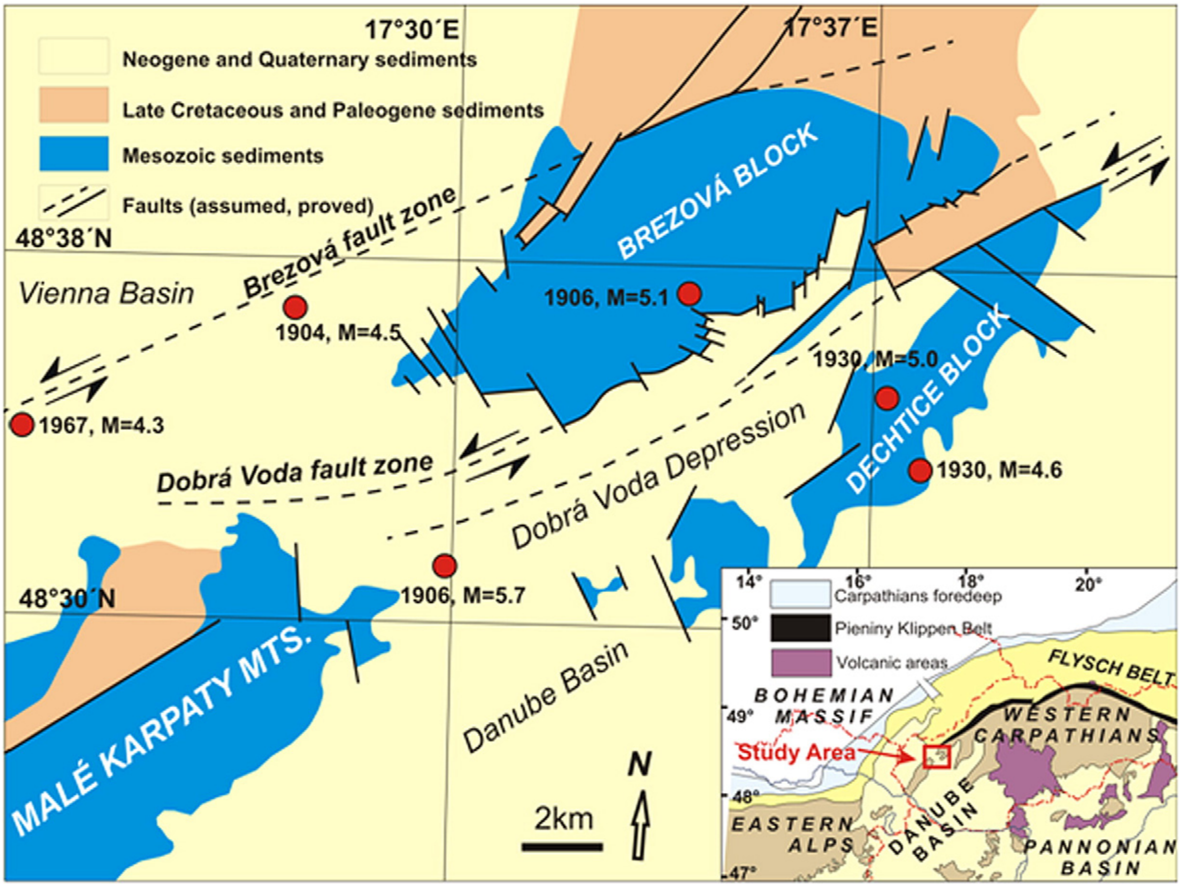

Fig. 2. A simplified geological sketch of the Eastern Alp – Western Carpathians region together with a detailed tectonic map of the Dobrá Voda seismic zone and the surrounding area (modified after Began et al., 1984; Marko et al., 1991). The red full circles show the approximate epicentres of the strongest earthquakes that occurred in this area during the last century.

3.1. Inversion from polarities of P waves

Double-couple focal mechanisms of the analyzed events were calculated using the Focmec code (Snoke, 2003). We inverted the polarities of P waves observed at local stations and the polarities of Pg and Pn waves observed at some of the nearest regional stations. The angles of incidence were calculated by ray tracing. In order to calculate also the rays of refracted Pg waves, the layered velocity model (see Table 2) was smoothed in depths above the Moho discontinuity into a gradient model (see Fig. 5). Satisfactory double-couple solutions defined by the strike, dip and rake angles were sought in the grid over the whole range of angles in steps of 5°. We accepted a different number of erroneous polarities for each event (see Table 3). In most cases, we accepted 1–2 errors in polarities in dependence on the total number of measured polarities and on the complexity of the P waveforms. For events with polarities measured also at regional stations and for events with a complex waveform, the focal distribution of polarities was less consistent (indicated by presence of some randomly distributed opposite polarities in the same area of the focal sphere) and the number of erroneous polarities had to be increased. This applies, for example, to the strongest event (V03) with anomalously complex waveforms (see Fig. 3). For each event, we obtained a family of satisfactory solutions. The number and scatter of the solutions depended on the coverage of stations on the focal sphere. For a less favourable coverage, the focal mechanisms were not sufficiently constrained and the event had to be discarded (see Fig. 6). In this way, we obtained 16 events with well-constrained sets of focal mechanisms. The optimum solution of each well-constrained set of focal mechanisms was calculated as the average over the satisfactory solutions (see Table 3 and Fig. 13). The accuracy of the optimum solution was roughly estimated by an average deviation of P and T axes of each set of focal mechanisms.

3.2. Inversion from amplitudes of P waves

The P waves amplitudes were measured from the displacement records observed at local stations with epicentral distance up to 80 km. The amplitudes of P waves observed at more distant stations were excluded, because their ray-theoretical modelling is complicated. For example, the amplitudes of the Pn waves cannot be calculated by the standard ray theory and their modelling requires a very accurate knowledge of the crustal model.

The analyzed records were filtered by applying a high-pass filter with the corner frequency of 1 Hz to remove low-frequency noise. The first maximum of the vertical component of the P wave was measured (see Fig. 7), The amplitudes of P waves measured at the horizontal components were not utilized in the inversion because they were more noisy and did not bring any new information into the inversion. The Green functions were calculated using the ray method (Červený, 2001). In order to calculate also refracted waves, the layered velocity model (see Table 2) was smoothed into a gradient model (see Fig. 5) similarly as in tracing rays in the inversion from P-wave polarities. The ray amplitudes also incorporate the effects of the Earth's surface.

The moment tensors were calculated using the AMT computer code written in Matlab (Vavryčuk, 2009). The code combines ray

Table 1
List of events.

ID	Focmec	AMT	Isola	Date	Time	*Mw*	Latitude [°]	Latitude error [km]	Longitude [°]	Longitude error [km]	Depth [km]	Depth error [km]
Q01			x	21.1.2001	05:30:03.51	1.8	48,667	0.7	17,438	0.6	1.1	0.5
Q02			x	1.3.2001	23:09:31.49	2.2	48,465	0.8	17,242	1.2	6.7	2.2
Q05			x	12.5.2001	18:24:24.91	1.8	48,692	0.6	17,523	0.3	8.1	0.6
Q08		x	x	4.6.2001	03:51:25.57	2.0	48,681	1.5	17,780	0.8	12.3	0.7
Q09		x	x	6.6.2001	20:33:12.02	2.4	48,647	1.5	17,801	0.9	11.5	1.1
Q11		x	x	28.6.2001	02:00:06.12	2.4	48,650	1.0	17,788	0.8	10.6	0.8
Q12			x	28.6.2001	02:36:17.56	2.4	48,649	1.5	17,814	1.1	8.8	1.7
Q13		x	x	8.9.2001	13:37:16.51	1.7	48,448	0.2	17,308	0.3	6.7	0.6
Q14		x	x	9.9.2001	17:05:00.87	1.8	48,540	0.3	17,630	0.3	1.6	0.2
Q15		x	x	10.9.2001	01:17:49.62	1.6	48,534	0.3	17,633	0.2	1.6	0.2
Q16		x	x	22.9.2001	07:48:39.73	1.8	48,571	0.1	17,454	0.2	7.2	0.3
R01		x	x	15.5.2002	13:57:23.27	1.9	48,578	0.7	17,729	0.9	1.2	0.4
R02		x	x	8.8.2002	20:05:49.71	2.2	48,578	0.5	17,127	0.4	6.5	0.8
R03	x	x	x	15.12.2002	11:04:48.46	2.6	48,522	0.2	17,490	0.1	5.6	0.2
S01		x	x	28.2.2003	16:04:08.74	1.7	48,432	0.5	17,354	0.5	3.1	0.2
S02	x	x	x	5.4.2003	20:21:39.11	2.6	48,561	0.5	17,426	0.3	7.3	0.6
S03	x	x	x	17.6.2003	08:58:16.21	2.8	48,592	1.2	17,718	1.3	12.1	1.3
S04			x	26.8.2003	10:28:36.49	2.0	48,340	1.9	17,139	2.8	9.3	3.8
T01		x	x	29.4.2004	07:47:11.31	1.5	48,518	0.4	17,582	0.3	2.2	0.4
U01		x	x	16.11.2005	08:27:13.39	1.9	48,574	0.2	17,516	0.2	9.1	0.3
V03	x	x	x	13.3.2006	08:28:38.39	3.4	48,550	0.6	17,694	0.5	10.2	0.7
V04	x	x	x	14.3.2006	09:09:48.82	2.3	48,555	0.8	17,711	0.6	12.3	0.8
V05	x	x	x	14.3.2006	09:18:43.52	2.1	48,555	0.9	17,704	0.7	13.2	0.9
V06	x	x	x	14.3.2006	11:42:13.19	2.3	48,553	0.7	17,708	0.6	12.4	0.8
V07	x	x	x	14.3.2006	11:47:20.41	2.0	48,558	0.8	17,707	0.7	12.4	0.9
V08	x	x	x	19.4.2006	00:01:32.09	2.0	48,543	0.5	17,707	0.4	9.8	0.6
V09	x	x	x	20.4.2006	13:15:48.15	2.4	48,556	0.7	17,672	0.6	7.9	1.0
V20		x	x	5.8.2006	08:57:34.51	2.2	48,520	0.2	17,475	0.2	4.3	0.5
V13		x	x	5.8.2006	08:58:49.56	2.3	48,511	0.6	17,473	0.4	5.3	0.9
V14	x	x	x	5.8.2006	09:00:08.63	3.0	48,516	0.7	17,468	0.4	5.2	1.1
V15		x	x	5.8.2006	09:03:49.61	1.5	48,515	0.3	17,473	0.2	4.8	0.5
V16			x	5.8.2006	09:58:56.20	1.5	48,510	1.0	17,472	0.5	4.6	1.5
V17		x	x	5.8.2006	23:43:18.38	1.2	48,522	0.1	17,476	0.1	4.7	0.2
V18	x		x	13.10.2006	01:01:15.09	2.5	48,591	0.8	17,190	0.8	9.3	1.0
V19	x	x	x	25.10.2006	23:54:13.09	2.1	48,571	0.7	17,720	0.5	11.1	0.6
W01	x	x	x	10.1.2007	21:43:17.25	1.9	48,478	0.8	17,329	0.3	3.0	0.2
W02		x	x	11.1.2007	22:50:21.40	1.9	48,568	1.9	17,283	1.1	5.1	3.6
W03	x			27.2.2007	17:11:41.01	2.6	48,339	3.3	17,171	1.4	13.4	5.4
W05		x	x	4.8.2007	02:39:19.79	2.4	48,581	0.5	17,565	0.4	10.3	0.7
X01	x	x	x	27.3.2008	21:51:47.22	2.1	48,539	0.5	17,624	0.4	8.8	0.6
X02		x	x	30.3.2008	07:36:56.91	2.7	48,519	0.4	17,349	0.3	2.6	1.1
X03		x	x	25.2.2008	14:27:43.17	1.3	48,522	0.3	17,465	0.2	3.7	0.6
X04		x	x	25.6.2008	14:25:52.38	2.1	48,559	1.0	17,418	1.2	9.1	2.0
Y01		x	x	19.4.2009	10:16:56.08	2.6	48,549	0.2	17,374	0.2	6.1	0.3
Total	16	36	43									

ID is the identification code of the events, the 2nd, 3rd and 4th columns indicate which events have been inverted using the Focmec, AMT and Isola codes, respectively, *Mw* is the moment magnitude.

tracing in a smooth velocity model, calculation of the ray-theoretical Green functions (Červený, 2001) and the generalized linear inversion (Lay and Wallace, 1995). The stability of the moment tensors was tested by a repeated inversion of data contaminated by artificial noise. We calculated the moment tensors of 100 random realizations. The maximum noise level was 25% of the measured P-wave amplitude at each station. The probability distribution was uniform. In estimating the stability of the moment tensors, we focused on evaluating the percentage of the DC component of the optimum solutions inverted from noise-free data and on the scatter of the P/T axes and the nodal lines of the 100 solutions inverted from the random realizations of noisy data. The low percentage of the DC component and the high scatter of the P/T axes and of the nodal lines were an indicator of probably unstable and less accurate inversion (see Fig. 8). Based on the stability of the inversion we classified the moment tensors as reliably or unreliably determined. The reliable moment tensors were selected using the two following criteria: (1) The percentage of the DC component was required to be higher than 40%, and (2) the mean deviations of the P/T axes of the 100 random realizations from the P/T axes of the optimum solutions obtained from the noise-free data did not exceed 5°.

The results for the whole dataset of 36 analyzed events are summarized in Table 4, where the reliably determined moment tensors are highlighted. The table presents the root mean square (RMS) value of amplitude errors calculated by the following formula:

$$\mathrm{RMS} = \frac{\sqrt{\sum_{i=1}^{N}\left(A_{obs}^{(i)} - A_{teor}^{(i)}\right)^2}}{\sqrt{\sum_{i=1}^{N}\left(A_{obs}^{(i)}\right)^2}},$$

where A_{obs} and A_{teor} are the observed and theoretical P-wave amplitudes, superscript i is the number of the station, and N is the total number of stations at which the amplitudes were measured for the respective earthquake. The table lists also the ratio of the minimum to maximum eigenvalues of the inverted matrix (min/max ratio), the percentage of the non-DC components and their errors calculated as standard deviations of the 100 solutions inverted from random realizations of noisy data. The reliably determined focal mechanisms are also shown in Fig. 13.

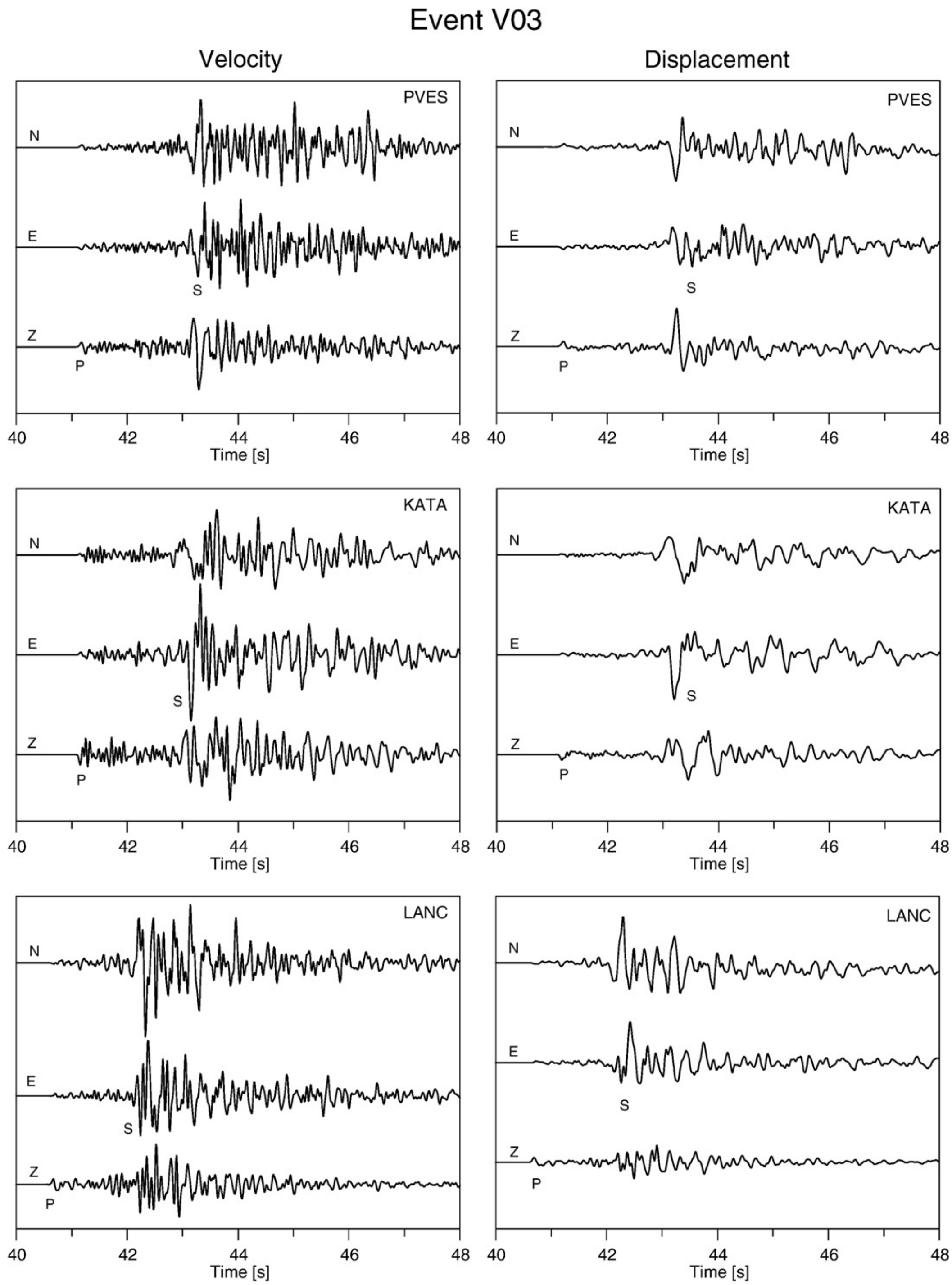

Fig. 3. Velocity (left-hand plots) and displacement (right-hand plots) records of the strongest analyzed event V03 recorded at stations PVES, KATA and LANC.

3.3. Inversion from waveforms

The waveform inversion was performed using the Isola computer code developed by Sokos and Zahradník (2009). The Isola code combines a user-friendly interface written in Matlab with an inversion engine written in Fortran. The inverse problem is formulated after Kikuchi and Kanamori (1991). The match between the observed and best-fitting synthetic data is characterized by the overall variance reduction. The code allows inverting for complex rupture histories with multiple point-source sub-events. Applications of the Isola code to the retrieval of moment tensors of regional earthquakes can be found, for example, in Zahradník et al. (2005, 2008a,b) and Adamová et al. (2009).

We inverted for full moment tensors from the displacement records from 3 to 5 nearest local stations. The stations at small epicentral distance were chosen because they displayed simplest waveforms thus being less affected by structural complexities than the far distant stations. The inverted records were pre-processed by high-pass filtering with a corner frequency of 0.4 Hz to remove microseisms and offset. Subsequently, the records were re-sampled from a frequency of 100 Hz to 33 Hz and corrected for the transfer function of the seismometer. The seismograms were checked to have

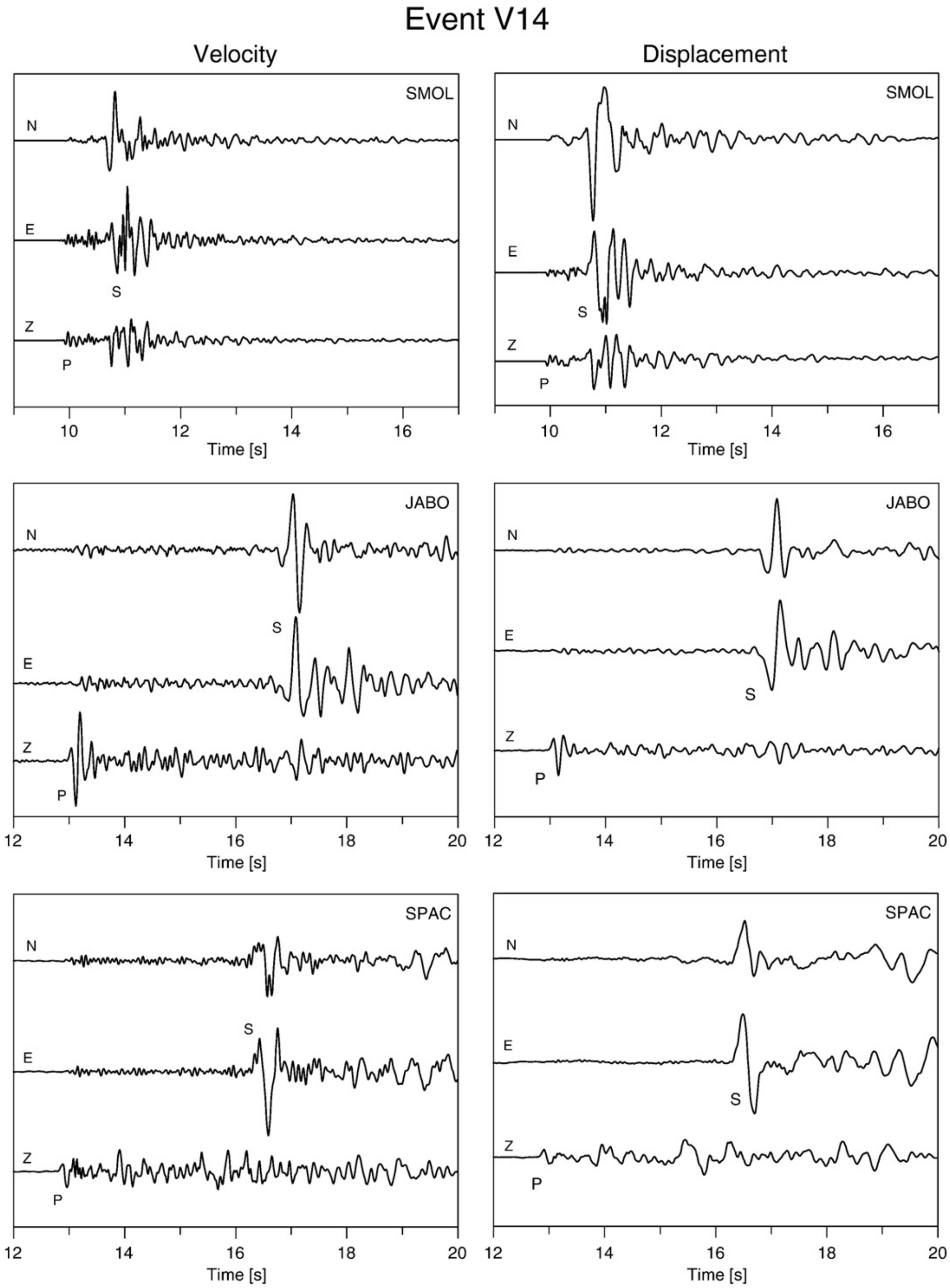

Fig. 4. Velocity (left-hand plots) and displacement (right-hand plots) records of the second strongest analyzed event V14 recorded at stations SMOL, JABO and SPAC.

Table 2
1-D velocity model of the crust.

Layer	Depth [km]	v_P [km/s]	Q_P	Q_S
1	0.0	4.0	200	100
2	1.9	4.8	200	100
3	2.5	5.6	300	150
5	4.5	6.0	300	150
6	10.0	6.2	500	250
7	30.0	8.2	800	400

v_p is the P-wave velocity, Q_P and Q_S are the quality factors of P and S waves.

a sufficiently high signal-to-noise ratio. The theoretical and observed waveforms were further filtered by a band-pass filter with corner frequencies of 0.8 Hz and 1.6 Hz. This rather narrow-band filtering was used to extract a low-frequency content of the S waves and surface waves. These waves are less sensitive to the complexities in the seismic structure and yield more stable results compared with the inversion of the high-frequency waveforms. The Green functions were calculated using the discrete-wave-number method (Coutant, 1990; Bouchon, 2003). In calculating the Green functions, the positions of epicentres were fixed (see Table 1). Since the depths of foci are the most uncertain parameter, the depth was allowed to deviate from the

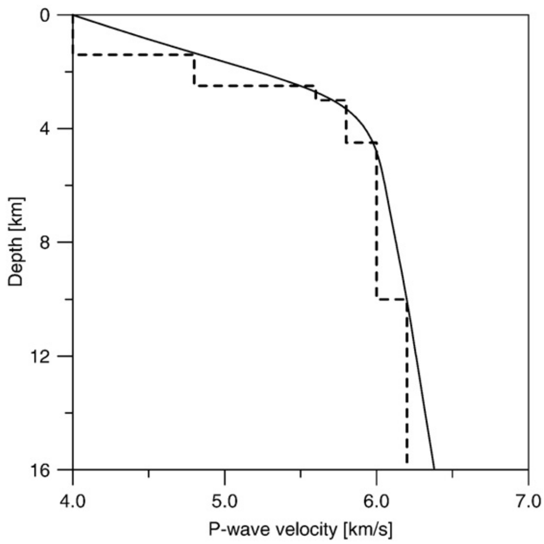

Fig. 5. P-wave velocities in the 1-D layered (dashed line) and gradient (solid line) models. The layered model is used in the location procedure and for calculating synthetic waveforms using the wave-number method. The gradient model is used in ray tracing and for calculating synthetic ray-theoretical P-wave amplitudes in the amplitude inversion.

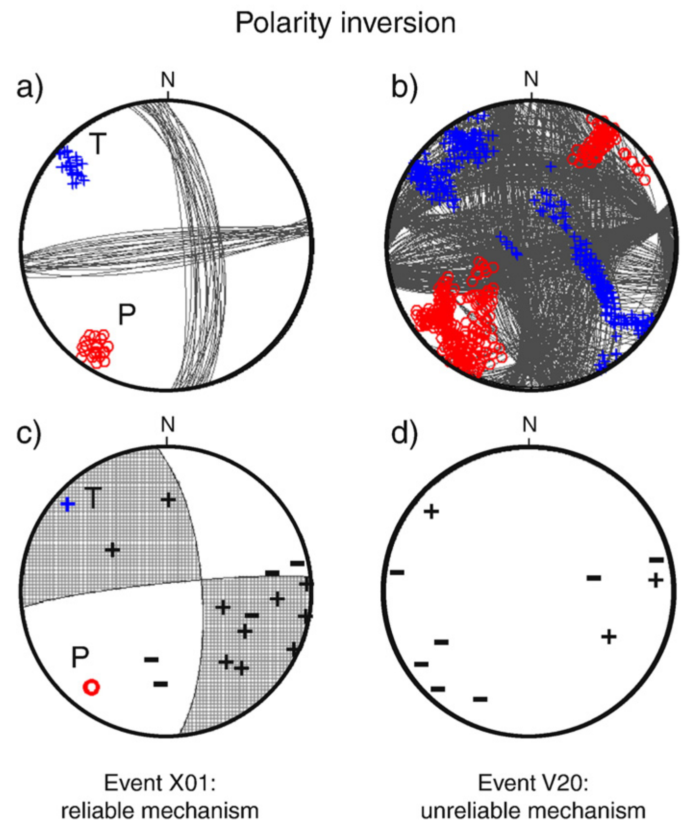

Fig. 6. Examples of reliable and unreliable focal mechanisms determined from the P-wave polarities The reliable focal mechanism is shown for event X01 (left-hand plots) and the unreliable focal mechanism is shown for event V20 (right-hand plots). (a–b) Nodal lines and P/T axes for the satisfactory solutions, (c–d) focal sphere coverage and the optimum focal mechanism. The scatter of solutions for event V20 prevents from determining the optimum solution. The P axes are marked by red circles and the T axes by blue plus signs.

optimum depth found in the location procedure by up to ±2.5 km in steps of 0.5 km. For shallow foci with depths less than 3.0 km, the depth ranged from 0.5 km down to 5.5 km. Similarly, the origin (centroid) time of the earthquake was allowed to vary up to ±1 s from that found by the location procedure. The time step in the grid search was identical with the sampling interval of 0.03 s. The inversion was performed at each depth and for each time shift, and the optimum solution was found as the solution with the best fit over all depths and times.

As an example, we show the results of the inversion for two events: event V14 with $Mw = 3.0$ (Figs. 9 and 10) and event W01 with $Mw = 1.9$ (Figs. 11 and 12). The figures show a comparison of observed and the best-fitting synthetic seismograms at four inverted stations, and the correlation coefficient between the observed and synthetic seismograms as a function of the position of the hypocentre and of the time shift.

The comparison of seismograms indicates that the fit between synthetic and observed waveforms is low, only the main features of the waveforms are fitted. As expected, the synthetic seismograms have simpler waveforms than the observed seismograms (see Figs. 9 and 11). In particular, the synthetic and observed waveforms differ at later times when observations become complex due to secondarily generated waves which cannot be produced in a simple velocity model. The low fit at later times is expressed by low numbers of variance reduction (see Table 5) and points to presence of a complex laterally inhomogeneous structure in the target area. Fortunately, a fit of waveforms at early times is more important for the success of the inversion. The misfit at later times decreased probably the accuracy of the results but did not lead to failure of the inversion.

Table 3
Focal mechanisms determined from the P-wave polarities.

No	ID	Total number of polarities	Number of erroneous polarities	Number of solutions	Optimum solution			Mean P-axis deviation [°]	Mean T-axis deviation [°]
					Strike [°]	Dip [°]	Rake [°]		
1	R03	20	0	5	242	81	−36	7.8	7.5
2	S02	12	0	12	87	67	69	5.7	7.1
3	S03	20	2	6	255	59	−13	6.4	6.6
4	V03	33	8	92	241	82	18	15.4	8.3
5	V04	16	1	18	92	77	37	8.3	7.7
6	V05	12	1	71	286	78	−42	8.0	9.9
7	V06	12	1	99	98	75	49	9.1	12.1
8	V07	8	0	35	271	73	−40	6.8	7.1
9	V08	9	0	12	127	84	−117	5.1	5.1
10	V09	13	1	88	308	74	−76	10.4	13.7
11	V14	17	2	27	58	84	82	5.2	5.6
12	V18	15	2	17	330	81	58	7.3	16.3
13	V19	17	2	54	277	72	8	12.4	10.2
14	W01	8	0	55	284	68	9	18.5	15.8
15	W05	16	2	44	87	78	−21	10.0	14.9
16	X01	15	1	21	264	85	−20	5.2	4.8

The correlation coefficient depends on depth of the focus and is periodical with respect to the time shift (see Figs. 10 and 12). The dependence on depth is rather slight, so the procedure cannot be used to increase the depth accuracy of the focus. However, the periodicity with respect to the time shift is more pronounced. This is caused by inverting seismograms of a rather narrow frequency band. The optimum solutions corresponding to the maxima of the correlation coefficient are mutually very similar; they just differ in the sign of the moment tensor. This indicates that the waveform inversion is usually capable to retrieve a stable mechanism but it cannot safely retrieve its sign. Since rather narrow frequency-band waveforms are inverted, the inversion is almost insensitive to the actual first-motion polarities and it can produce moment tensors of an incorrect sign. Therefore, the plus/minus signs of the resultant moment tensors were checked after the inversion and corrected to predict the true first-motion polarities of the local P waves. In checking the sign of the moment tensors, we required the number of the correctly predicted P-wave polarities to be higher by at least 2 than that of the incorrectly predicted polarities. The moment tensors which did not satisfy this polarity criterion were considered as unreliable and were discarded.

Similarly as in the amplitude inversion, we tried to assess the stability of the inversion and to estimate the reliability of the retrieved moment tensors. We used the following criteria for selecting the reliably determined moment tensors: (1) similarly as in the amplitude inversion, the percentage of the DC component was required to be higher than 40%, and (2) the min/max eigenvalue ratio of the inverted matrix had to exceed the value of 0.019. This value has been used to select approximately the same number of the reliably determined moment tensors as in the moment tensor inversion from amplitudes. Since the waveform inversion was more computationally demanding than the amplitude inversion, we did not perform repeated inversions with noisy input data as we did in the amplitude inversion.

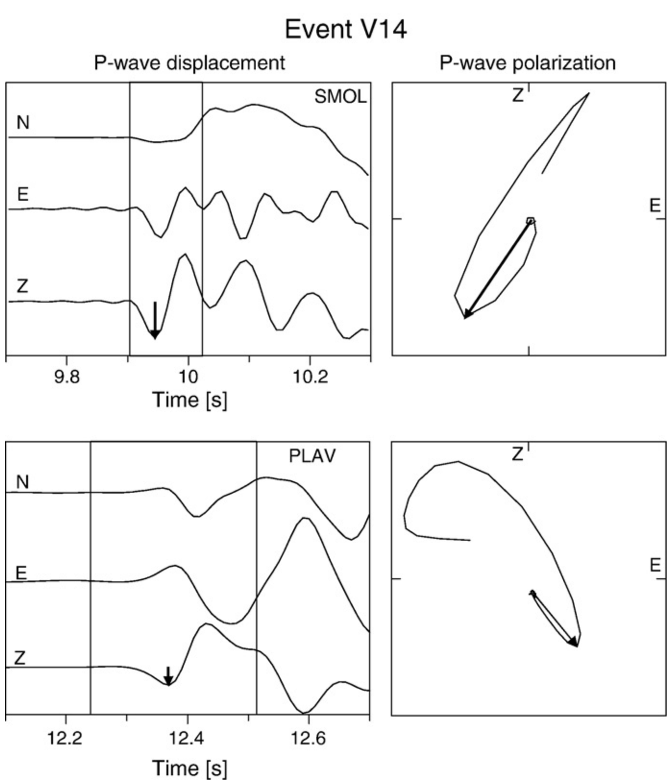

Fig.7. Picking of P-wave amplitudes for event V14 recorded at stations SMOL and PLAV. The vertical lines at the displacement records (left-hand plots) delimit the time interval shown in particle motions (right-hand plots). The arrow marks the P-wave amplitude used in the inversion.

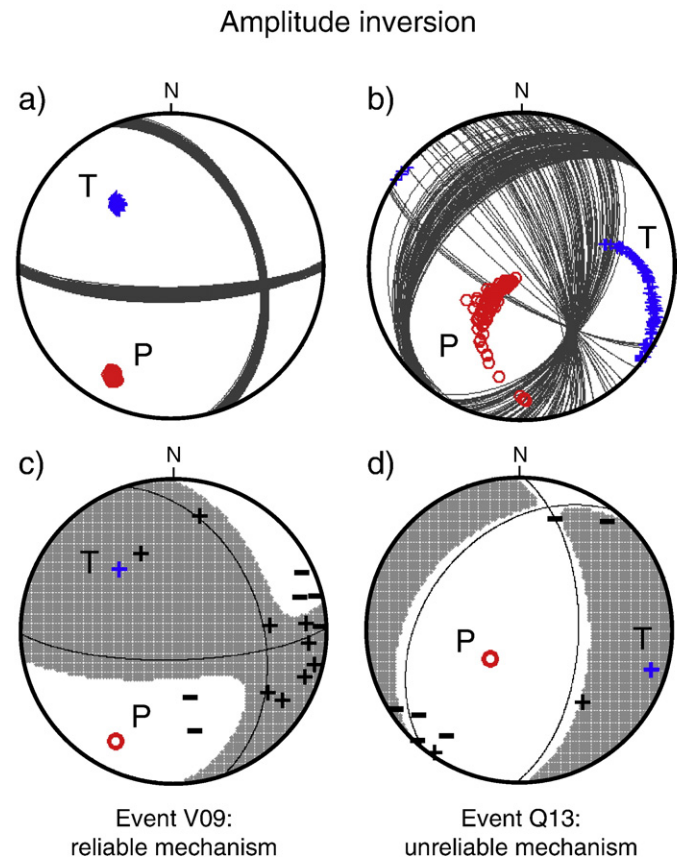

Fig. 8. Examples of reliable and unreliable focal mechanisms determined from amplitudes of P waves. The reliable focal mechanism is shown for event V09 (left-hand plots) and the unreliable focal mechanism is shown for event Q13 (right-hand plots). (a–b) Nodal lines and P/T axes for 100 solutions obtained from the inversion of P-wave amplitudes contaminated by random noise. (c–d) Focal sphere coverage and the optimum focal mechanisms. The dashed area shows the directions of the positive P axes polarity. The P axes are marked by red circles and the T axes are marked by blue plus signs.

We inverted 43 events in total (see Table 5) but 8 events did not satisfy the polarity criterion and had to be discarded. From 35 events which fulfilled the polarity criterion, the 15 events were selected as those with reliably determined moment tensors. These events are highlighted in the Table and their focal mechanisms are shown in Fig. 13.

3.4. Comparison of the results

Fig. 13 shows individual reliably determined focal mechanisms calculated using: (1) polarities of the Pg, Pn and local P waves, (2) amplitudes of local P waves, and (3) complete waveforms observed at local stations. Fig. 14 shows the nodal lines and the P/T axes of the DC parts of the respective three sets of the focal mechanisms. While the individual focal mechanisms determined by different methods can differ for some of events, the three sets of the nodal lines and the P/T axes display a statistically similar pattern. In all three inversions, the majority of mechanisms have the P axes clustered in the SW-NE direction close to the horizontal plane. The T axes are more scattered but still predominantly in the NW-SE direction and mostly incline from the horizontal plane. Since the three sets of the focal mechanisms were calculated using different methods with different input data, they can be considered as independent and their overall consistency validates the correctness and good accuracy of the inversions.

The predominant focal mechanisms are strike-slips with a small normal or reverse component with strikes around 0° or 180°. Some mechanisms have strikes around 60° or 240° corresponding to the

Table 4
Moment tensor inversion from the P-wave amplitudes.

ID	Number of stations	RMS	Ratio min/max	Strike [°]	Dip [°]	Rake [°]	Mean P-axis deviation [°]	Mean T-axis deviation [°]	DC [%]	CLVD [%]	ISO [%]	Error DC [%]	Error CLVD [%]	Error ISO [%]
Q08	8	0.13	5.2E–04	288	89	93	6.6	3.7	24.0	47.2	28.9	4.6	3.5	1.4
Q09	8	0.23	3.7E–04	43	85	80	13.4	5.7	40.8	39.1	20.1	16.4	13.4	8.5
Q11	8	0.65	9.9E–05	285	56	139	70.5	1.9	17.8	59.9	22.3	6.7	4.8	3.5
Q13	8	0.39	6.9E–05	1	58	−112	11.5	22.0	61.9	−25.0	−13.1	13.7	28.5	2.7
Q14	7	0.10	3.0E–04	97	64	−66	18.6	8.7	70.8	19.3	−9.9	17.0	30.4	15.4
Q15	8	0.16	3.3E–03	114	83	−45	5.6	2.9	65.2	32.1	2.7	6.2	6.7	2.9
Q16	8	0.09	1.2E–02	32	57	−126	2.0	33.1	70.8	16.1	13.1	9.3	5.9	3.9
R01	8	0.11	1.1E–05	137	81	101	8.7	3.9	5.3	62.0	32.7	4.3	3.4	1.0
R02	8	0.06	1.7E–04	128	48	105	19.4	1.8	16.9	53.1	30.0	2.3	2.0	0.4
R03	15	0.32	2.2E–02	256	89	−53	3.8	3.6	55.0	25.9	19.2	7.0	5.2	2.3
S01	8	0.29	2.7E–05	72	65	53	8.0	2.5	9.9	59.1	31.0	2.7	3.9	1.2
S02	16	0.38	8.1E–02	11	71	−153	2.7	2.1	48.3	36.3	15.4	8.6	6.5	2.2
S03	21	0.26	1.4E–02	74	59	60	1.2	0.9	59.8	21.6	18.7	5.0	4.5	0.8
T01	7	0.20	1.5E–04	351	70	−112	1.6	1.6	53.5	−28.2	−18.3	3.8	2.4	1.4
U01	8	0.29	1.1E–02	243	73	−159	1.7	3.1	70.6	15.8	13.7	4.4	3.9	1.2
V03	21	0.10	2.9E–02	310	85	113	5.2	6.7	46.6	−42.5	−10.8	9.9	7.8	2.8
V04	13	0.45	8.1E–04	105	84	49	1.0	1.1	34.9	40.8	24.3	6.4	5.1	1.3
V05	10	0.43	6.8E–04	101	85	46	1.5	1.8	49.4	29.2	21.4	11.1	8.7	2.4
V06	13	0.51	8.5E–04	102	84	49	1.4	1.5	38.5	38.3	23.3	8.3	6.5	1.8
V07	9	0.41	7.1E–04	102	86	50	1.4	1.6	42.3	35.1	22.7	11.1	8.7	2.4
V08	11	0.07	2.2E–02	84	74	−105	4.5	3.0	63.4	−21.3	−15.3	10.1	6.8	3.5
V09	15	0.13	5.2E–02	89	74	50	1.8	1.8	50.5	29.2	20.4	6.6	5.5	1.2
V13	11	0.36	2.9E–02	242	60	−46	6.7	21.2	46.8	45.8	−7.3	16.3	15.4	6.7
V14	12	0.52	3.4E–02	338	84	148	3.5	3.8	77.8	6.4	15.8	10.5	15.9	2.6
V15	8	0.29	5.0E–03	36	57	−58	8.3	22.8	70.7	10.0	−19.4	15.3	30.0	4.9
V17	7	0.07	3.8E–03	248	78	−48	11.1	11.9	62.3	29.8	7.8	10.4	10.3	6.4
V19	14	0.39	8.4E–03	145	71	132	4.5	3.3	62.1	−6.6	−31.3	7.8	13.8	3.5
V20	10	0.28	1.0E–04	264	58	113	4.9	0.6	8.7	61.8	29.5	1.0	0.6	0.5
W01	8	0.13	1.2E–05	285	50	−75	3.3	7.1	13.1	−60.2	−26.6	8.0	4.9	3.3
W02	19	0.56	7.0E–02	250	90	9	2.2	2.1	83.3	10.8	6.0	8.0	7.8	1.9
W05	17	0.25	8.6E–02	83	68	32	1.5	2.3	82.9	1.7	15.4	3.9	6.4	1.4
X01	18	0.56	2.8E–03	128	49	80	15.2	3.9	60.8	20.1	19.1	13.5	21.3	3.2
X02	12	0.17	9.2E–03	17	51	−108	4.3	11.6	60.2	−10.5	−29.4	7.1	9.2	1.6
X03	8	0.08	2.8E–03	40	61	−114	7.1	17.5	29.9	−39.5	−30.6	8.7	9.0	1.5
X04	9	0.45	2.4E–02	251	68	−110	4.2	2.5	60.4	38.9	0.7	8.1	8.5	4.9
Y01	10	0.15	1.2E–02	283	63	45	3.4	1.8	13.8	53.6	32.6	1.6	1.7	0.3

The highlighted events are classified as events with reliably determined moment tensors.

direction of the main fault system in the region (see Fig. 2). They are oblique strike-slips or normal events.

4. Non-DC components

Non-DC components of moment tensors can be spurious or of true physical origin. The spurious non-DC components are numerical errors of the inversion being usually a product of a limited amount of inverted data, of the simplification of the velocity model, of a mislocation, a simplification of the rupturing process, or of noise present in the data (Šílený and Vavryčuk, 2002; Šílený, 2009; Adamová and Šílený, 2010). However, the non-DC components may also be physical reflecting the properties of the earthquake source or of the medium in the focal area (Frohlich, 1994; Julian et al., 1998; Miller et al., 1998; Vavryčuk, 2001, 2005; Vavryčuk et al., 2008). The true physical non-DC components can be manifested, for example, by a positive correlation between the ISO and CLVD. The positive correlation between the ISO and CLVD can be an indicator of the presence of tensile faulting (see Vavryčuk, 2001). In this model, the positive values of ISO and CLVD are produced by opening of faults, while the negative values of ISO and CLVD are produced by closing of faults. The model of tensile faulting predicts a linear dependence between the ISO and CLVD percentages, the ISO/CLVD ratio being a function of the local value of the v_P/v_S ratio in the source area (see Vavryčuk, 2001, Eq. (17)).

The reliably determined moment tensors retrieved using the amplitude and waveform inversions were decomposed into their double-couple (DC) and non-double-couple (non-DC) components according to formulas of Vavryčuk (2001, Eqs. (8a–c)) or Vavryčuk (2005, Eqs. (15–17)). The histograms of the non-DC components are shown in Fig. 15. A significant part of the non-DC components is probably caused by numerical errors generated by the moment tensor inversions. This is evident, particularly, for the waveform inversion (see Fig. 15, right-hand plots) which produced highly scattered values of the non-DC components. Moreover, the ISO and CLVD are not well correlated. The correlation coefficient is 0.48 (see Table 6) which cannot be considered as significant. However, the amplitude inversion produces non-DC components with a significantly less scatter (see Fig. 15, left-hand plots) and also the correlation between the ISO and CLVD is higher attaining a value of 0.74 (see Table 6). The majority of events display positive ISO and CLVD, which is consistent with a model of tensile faulting during which the faults are slightly opening. Only 3 of 14 events have a significant negative ISO and CLVD having probably an anomalous or erroneous mechanism. From this viewpoint, the amplitude inversion seems to be more accurate than the waveform inversion, producing the non-DC components, which are probably more reliable and less affected by numerical errors. Adopting the model of tensile faulting, the v_P/v_S ratio is estimated to be 1.5, which is a reasonable value.

5. Tectonic stress

Tectonic stress is determined from focal mechanisms by applying the Angelier inversion method (Angelier, 2002). This method is a modification of the Gephart and Forsyth (1984) method and it is based on maximizing the so-called slip shear stress component (SSSC). Using the SSSC criterion is advantageous, because it avoids the

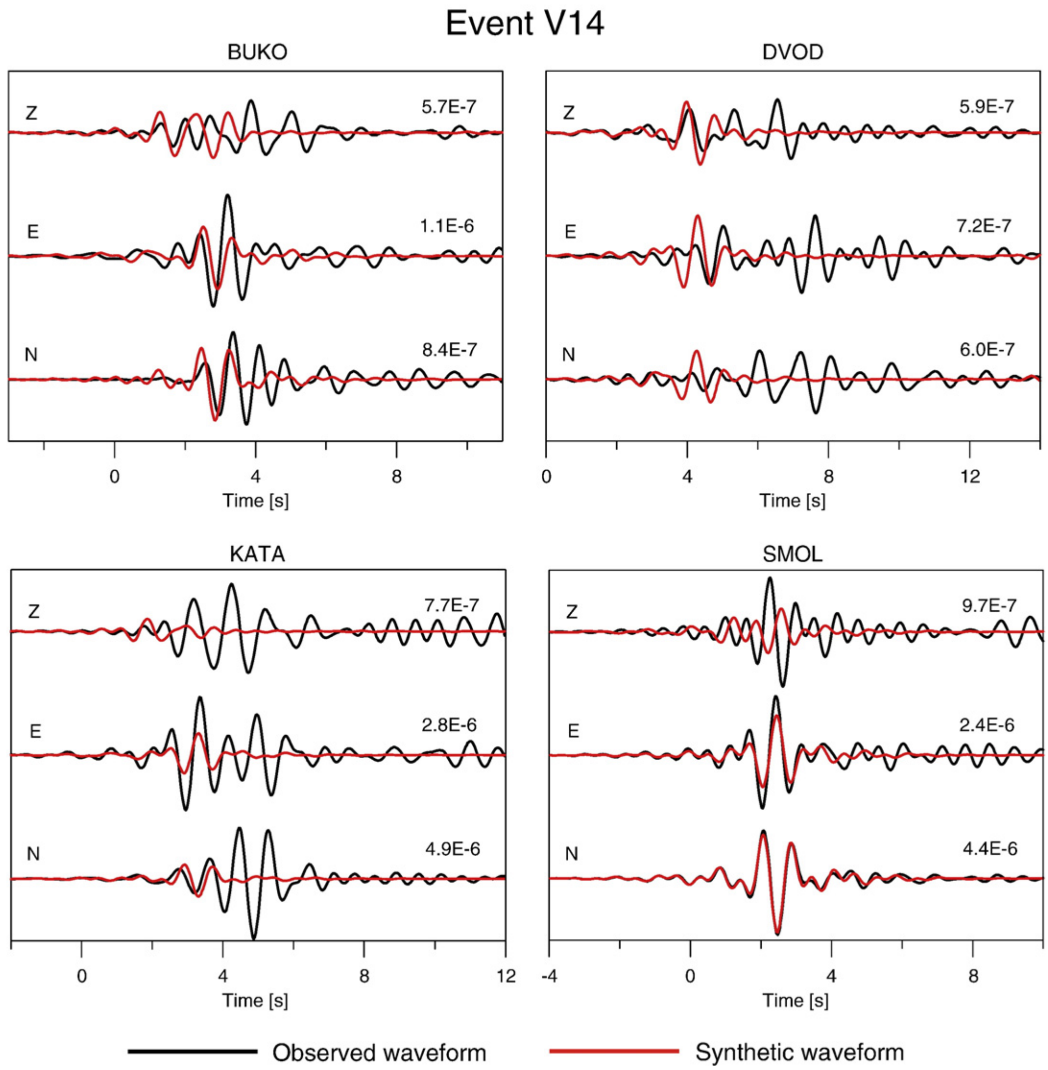

Fig. 9. Waveform inversion for event V14: a comparison of synthetic (red line) and observed (black line) waveforms at stations BUKO, DVOD, KATA and SMOL. The numbers at traces show their scale in metres.

necessity to identify the fault plane with one of the two nodal planes of each focal mechanism in the inversion. The SSSC function is maximized using the robust grid search inversion scheme. The approach recovers four parameters of the stress tensor: three angles defining the directions of the three principal stresses, σ_1, σ_2 and σ_3, and the shape ratio R, $R=(\sigma_1-\sigma_2)/(\sigma_1-\sigma_3)$. The approach is unable to recover the trace of the stress tensor $\sigma^{ISO}=\sigma_1+\sigma_2+\sigma_3$ and the magnitudes of the principal stresses.

We inverted for the tectonic stress in the Dobrá voda area from three different datasets: (1) DC focal mechanisms calculated using the P-wave polarities (Focmec, 16 well-constrained mechanisms, see Table 3), (2) the DC parts of the moment tensors calculated from the P-wave amplitudes (AMT, 14 reliably determined moment tensors, see Table 4), and (3) the DC parts of the moment tensors calculated from the complete waveforms (Isola, 15 reliably determined moment tensors, see Table 5). The inversion was performed using a 5° grid in searching for the principal stress directions and a 0.02 increment in searching for σ_2. The trace of the stress tensor was assumed to be zero and σ_1 was set to be 1. The results of the inversion are shown in Fig. 16 and summarized in Table 7. All three inversions yield similar results: the orientations of the principal stresses are (azimuth/plunge): $\sigma_1=210–220°/5–25°$, $\sigma_2=70–105°/55–75°$, and $\sigma_3=305–315°/15–25°$, and the shape ratio is $R=0.45–0.60$. The azimuth is measured clockwise from the north and the plunge is measured downwards from the horizontal plane. The consistency and low scatter of the results obtained using different data sets indicate that the principal stress directions are retrieved reliably and with high accuracy.

6. Tectonic implications

Comparing the tectonic sketch of the Dobrá Voda area (Fig. 2) with the predominant directions of the nodal lines of the focal mechanisms (Figs. 13 and 14), we conclude that some of the analyzed earthquakes occurred along the ENE–WSW trending fault system, This concerns particularly the strongest analyzed earthquakes (V03, V14, R03 and S03). However, a significant number of earthquakes occurred on faults or subfaults differently oriented than the main fault system. This indicates that the area is tectonically complex. The predominant faulting is the left-lateral strike-slip with minor normal or reverse components. The presence of non-DC components with prevailingly positive CLVD and ISO components revealed in the amplitude moment tensor inversion indicates that some earthquakes were not pure shear but probably combined shear and tensile faulting. It would point to high pore fluid pressure or to an extensional stress regime in the area.

Fig. 17 shows the orientation of the present-day tectonic stress calculated from the focal mechanisms under study together with other stress measurements in the Western Carpathians region and adjacent

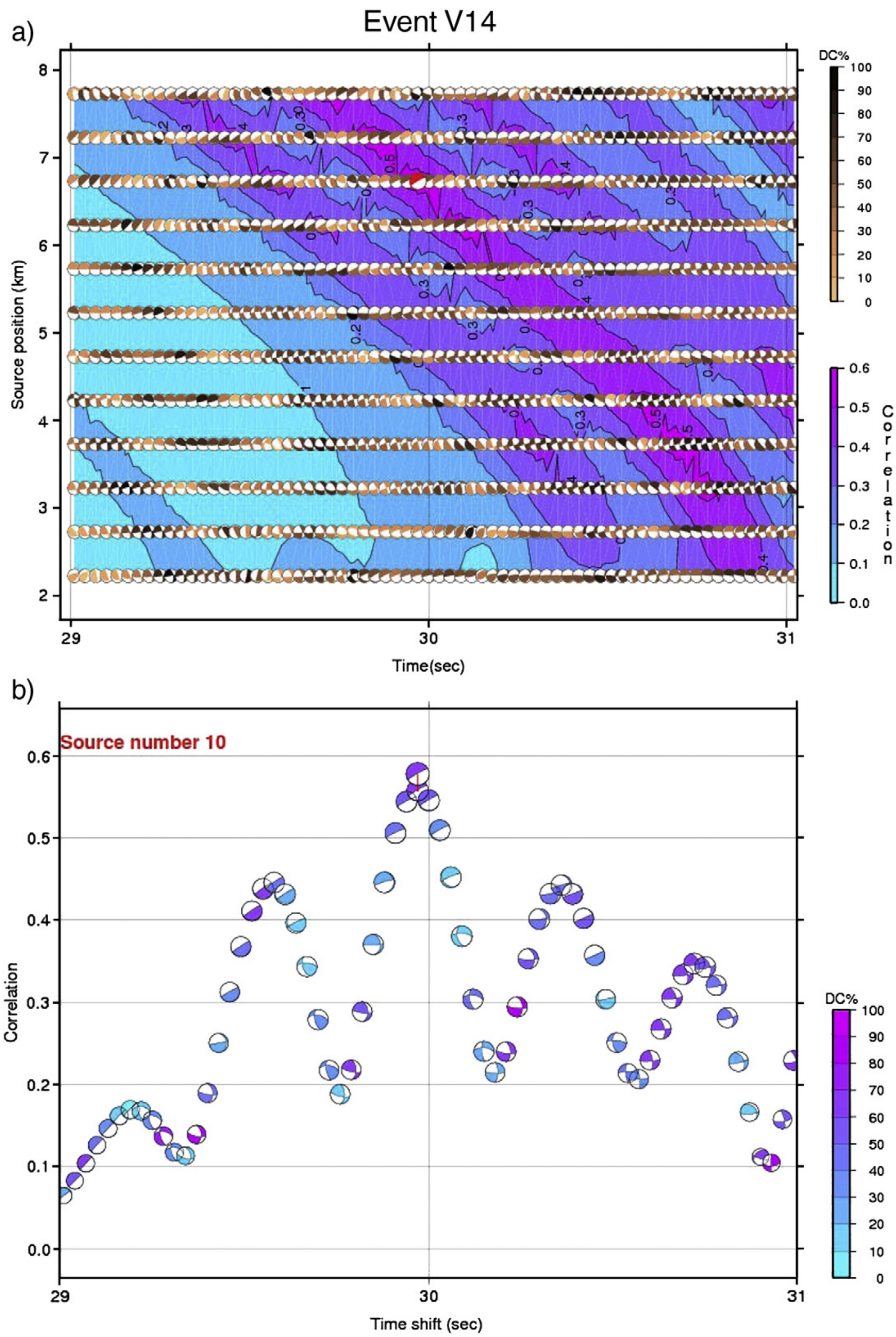

Fig. 10. Waveform inversion for event V14: the correlation coefficient and the corresponding focal mechanism as a function of (a) the time shift and source depth, and (b) the time shift at the optimum source depth. The correlation coefficient and the DC percentage in the corresponding focal mechanism are colour-coded. The origin time found using the location procedure has value 30 s. In the upper plot, the optimum solution is shown in red colour.

areas, downloaded from the World Stress Map web site (Müller et al., 1992; Heidbach et al., 2008). As indicated in the figure, the area under study lies in the transition zone between the Western Carpathians and Eastern Alps and is probably characterized by a complicated stress pattern (Drimmel and Trapp, 1982; Jarosinski, 1998; Reinecker, 2000; Kováč et al., 2002; Jarosinski, 2005). The retrieved maximum compression in the Dobrá Voda area has an azimuth of 210–220°NE and lies along the strike of the Malé Karpaty Mts. (see Fig. 17). The maximum compression direction is in coincidence with the measurements of the paleo-stress performed in the Malé Karpaty Mts. corresponding to the late Miocene to Pliocene periods (Nemčok et al., 1989). However, the paleo-stress analyses also show that the evolution of tectonic stress in the region was complex having been rotated, for example, during the Miocene period (Marko et al., 1991; Fodor, 1995). The complexity of the stress interpretations in the Malé Karpaty Mts. and adjacent areas is manifested also by the fact that some authors predict a character of the present-day stress field in this area (Hók et al., 2000; Kováč et al., 2002) opposite to that found in our analysis. These interpretations are mainly based on analysis of non-seismic data or focal mechanisms of a few single earthquakes.

Acknowledgements

The authors thank two anonymous reviewers for their detailed reviews, J. Hók and M. Šujan for fruitful discussions and comments to the paper, J. Zahradník for providing the Isola code and for his kind advice in waveform inversions, T. Fischer for providing the Seisbase code, and J. Sekereš for providing the data from the local seismic network MKNET. This work was supported by the Slovak Research and Development Agency under the Contract No. APVV-0158-06 (project NEOTACT – Neotectonic activity of the Western Carpathians), by the Grant Agency of the Academy of Sciences of the Czech Republic, Grant No. IAA300120801 and by the European Community's FP7 Consortium Project AIM "Advanced Industrial Microseismic Monitoring", Grant Agreement No. 230669.

References

Adamová, P., Šílený, J., 2010. Non-double-couple earthquake mechanism as an artifact of the point-source approach applied to a finite-extent focus. Bull. Seismol. Soc. Am. 100 (2), 447–457. doi:10.1785/0120090097.

Adamová, P., Sokos, E., Zahradník, J., 2009. Problematic non-double-couple mechanism of the 2002 Amfilochia Mw5 earthquake, Western Greece. J. Seismol. 13, 1–12. doi:10.1007/s10950-008-9112-4.

Angelier, J., 2002. Inversion of earthquake focal mechanisms to obtain the seismotectonic stress IV — a new method free of choice among nodal lines. Geophys. J. Int. 150, 568–609.

Began, A., Hanáček, J., Mello, J., Salaj, J., 1984. Geological map of Myjavská pahorkatina upland, Brezovské and Čachtické Karpaty Mts. Dionýz Štúr Institute of Geology, Bratislava.

Bouchon, M., 2003. A review of the discrete wavenumber method. Pure Appl. Geophys. 160, 445–465.

Briestenský, M., Stemberk, J., Petro, L., 2007. Displacements registered around the 13 March 2006 Vrbové earthquake M = 3.2 (Western Carpathians). Geol. Carpath. 58 (5), 487–493.

Červený, V., 2001. Seismic Ray Theory. Cambridge University Press, Cambridge.

Cipciar, A., Labák, P., Moczo, P., Kristeková, M., 2002. Monitoring of seismic phenomena by national seismic stations network. Geologické práce, Správy 106. Publishing House D. Štúra, Bratislava, pp. 123–132 (in Slovak).

Coutant, O., 1990. Program of numerical simulation AXITRA. Laboratoire de Géophysique Interne et Tectonophysique Report, University of Joseph Fourier (in French).

Drimmel, J., Trapp, E., 1982. Earthquakes in Austria between 1971 and 1980. Sitzungsberichte-Oesterreichische Akademie der Wissenschaften, Mathematisch -Naturwissenschaftliche Klasse, Abteiling I. 191, pp. 73–102.

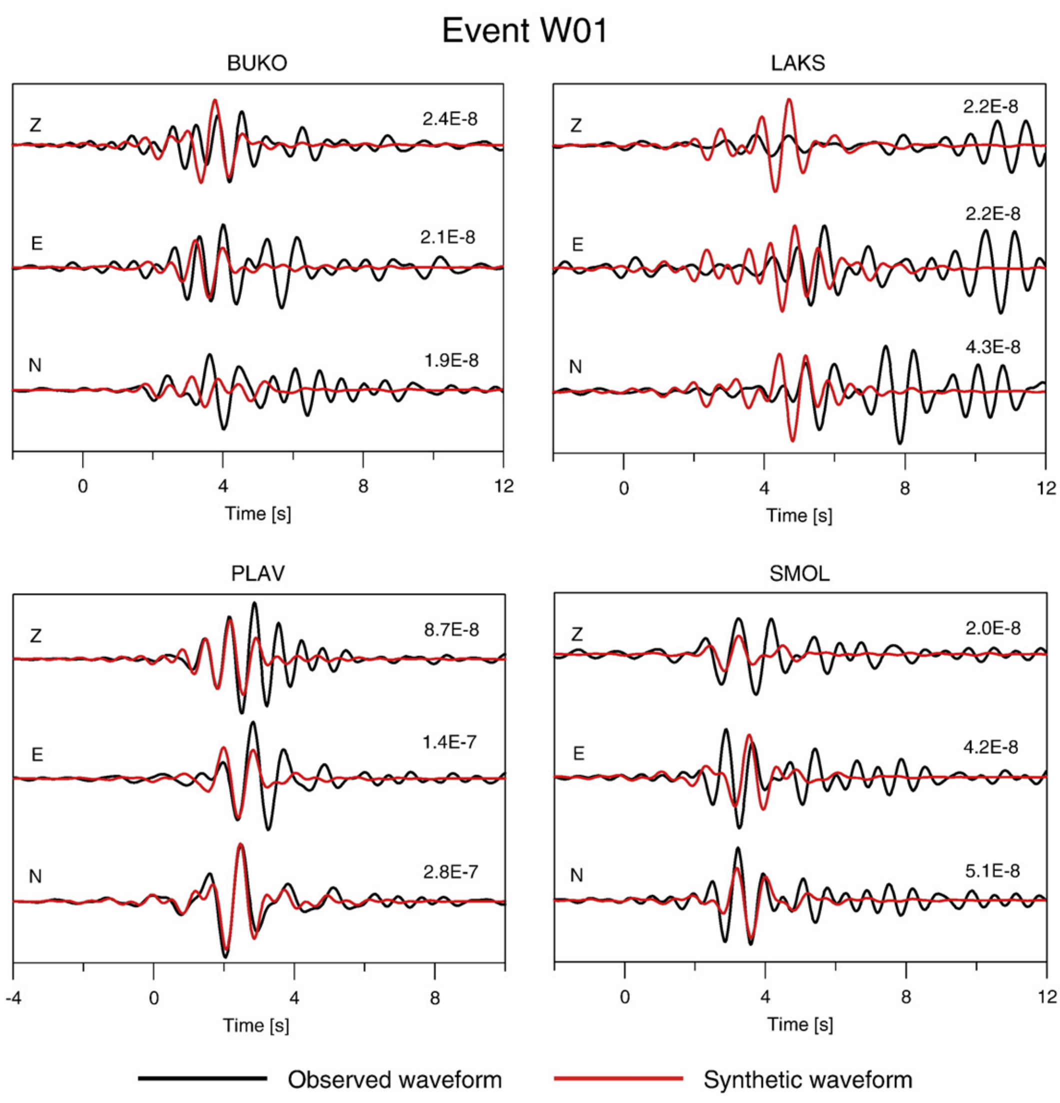

Fig. 11. Waveform inversion for event W01: a comparison of synthetic (red line) and observed (black line) waveforms at stations BUKO, LAKS, PLAV and SMOL. The numbers at traces show their scale in metres.

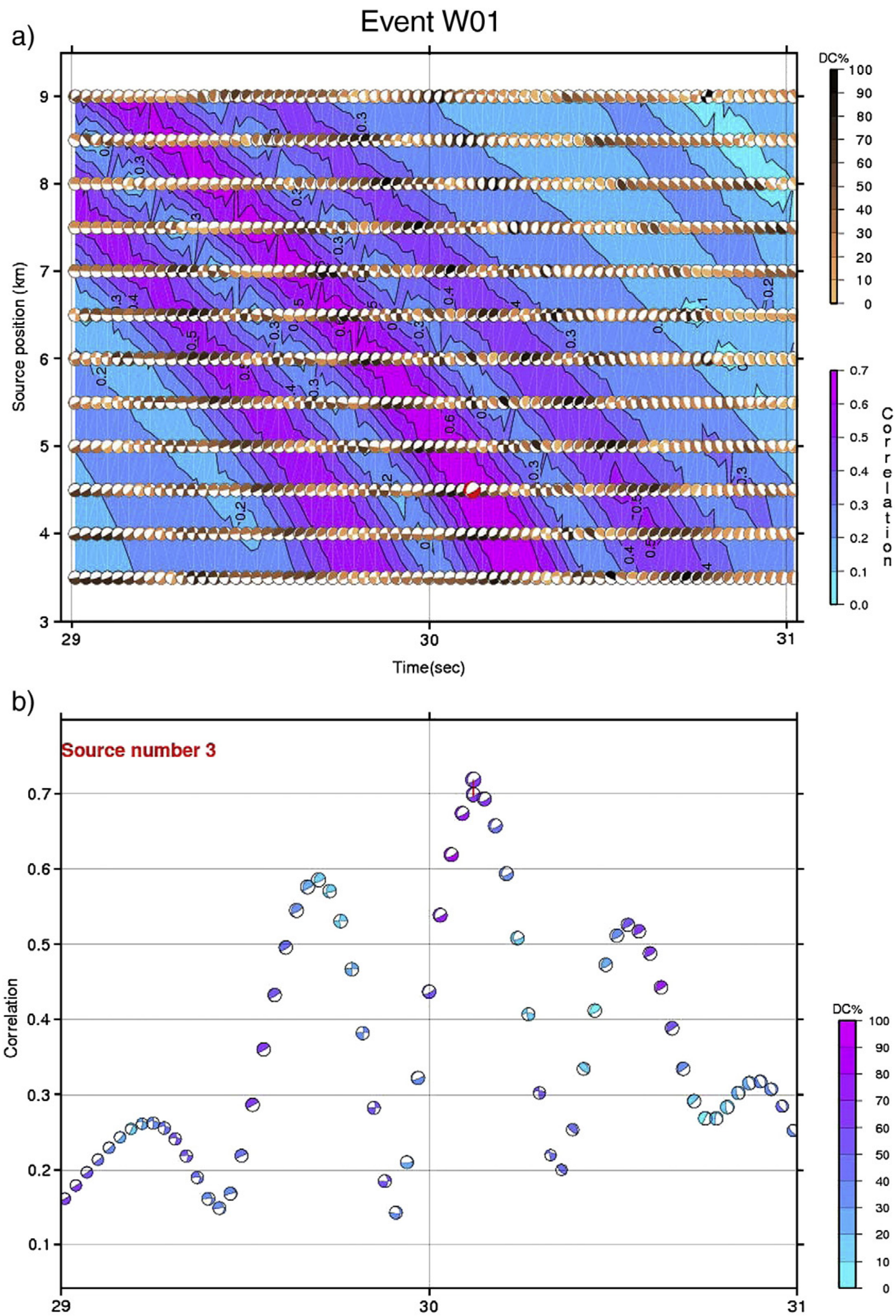

Fig. 12. Waveform inversion for event W01: the correlation coefficient and the corresponding focal mechanism as a function of (a) the time shift and source depth, and (b) the time shift at the optimum source depth. The correlation coefficient and the DC percentage in the corresponding focal mechanism are colour-coded. The origin time found using the location procedure has value 30 s. In the upper plot, the optimum solution is shown in red colour.

Fischer, T., Hampl, F., 1997. SeisBase — principles of a program and database for routine analysis of data from local seismic networks. Acta Montana A 11, 15–34.
Fodor, L., 1995. From transpression to transtension: Oligocene–Miocene structural evolution of the Vienna basin and the East Alpine-Western Carpathian junction. Tectonophysics 242, 151–182.
Frohlich, C., 1994. Earthquakes with non-double-couple mechanisms. Science 264, 804–809.
Gephart, J.W., Forsyth, D.W., 1984. An improved method for determining the regional stress tensor using earthquake focal mechanism data: application to the San Fernando earthquake sequence. J. Geophys. Res. 89, 9305–9320.

Table 5
Moment tensor inversion from waveforms.

ID	Number of stations	Variance reduction	Ratio min/max	Strike [°]	Dip [°]	Rake [°]	DC [%]	CLVD [%]	ISO [%]	*Mw*
Q01	4	2.74E–01	3.07E–02	54	72	−163	29.2	0.4	70.4	1.6
Q05	3	2.53E–01	2.22E–02	270	74	58	39.5	34.2	26.2	1.8
Q08	3	4.18E–01	8.45E–03	104	83	−55	37.8	19.7	42.4	2.0
Q09	4	3.91E–01	1.54E–02	115	84	−44	33.8	26.8	39.4	2.4
Q12	4	3.76E–01	1.27E–02	59	58	−120	12.0	56.9	31.0	2.4
Q13	4	2.67E–02	1.89E–02	58	70	−18	34.9	45.0	20.2	1.7
Q15	4	3.77E–01	2.24E–02	175	71	149	31.6	−34.5	−33.9	1.6
Q16	5	1.81E–01	3.49E–02	149	77	35	45.5	−41.4	−13.2	1.8
R01	3	6.04E–01	6.36E–02	108	83	−15	36.8	11.8	−51.4	2.0
R02	5	2.90E–01	2.08E–02	202	67	−67	16.9	−23.0	−60.1	2.2
R03	5	3.81E–01	3.89E–02	91	76	64	37.7	−18.4	43.9	2.7
S02	4	2.61E–01	3.27E–02	342	80	−158	68.1	−29.7	−2.2	2.4
S03	3	9.72E–02	2.61E–02	88	78	34	40.2	41.7	18.1	2.7
S04	4	2.28E–01	1.73E–02	211	62	−136	46.3	27.6	26.1	2.0
U01	4	2.96E–01	3.73E–02	149	79	−110	48.5	37.2	14.3	1.7
V03	4	1.03E–02	2.29E–02	286	74	115	22.9	47.5	29.6	3.4
V04	4	3.21E–01	2.60E–02	94	75	26	48.9	−40.6	−10.5	2.2
V05	4	3.26E–01	2.63E–02	97	73	26	35.0	−44.8	−20.2	2.0
V06	4	2.25E–01	1.96E–02	96	71	26	79.8	−13.9	−6.3	2.3
V07	4	2.18E–01	1.97E–02	93	73	23	78.5	−17.6	3.8	2.1
V08	4	2.15E–01	2.28E–02	106	89	−34	50.7	−17.0	−32.3	1.9
V09	3	2.42E–01	3.06E–02	307	76	−130	46.3	−29.6	24.1	2.2
V13	3	3.08E–01	4.73E–02	74	87	−10	51.4	−23.6	25.0	2.1
V14	3	3.11E–01	3.35E–02	240	85	−94	64.6	5.2	30.2	2.8
V15	3	3.12E–01	2.86E–02	175	56	−130	39.1	−26.0	34.8	1.6
V18	4	1.19E–01	1.82E–02	51	81	175	14,4	74.4	11.2	2.4
V19	4	1.43E–01	2.35E–02	358	80	−64	65.9	−7.0	−27.1	1.9
V20	4	2.81E–01	3.23E–02	249	82	27	32.0	−9.0	59.0	2.1
W01	4	4.88E–01	3.48E–02	63	70	−67	69.5	25.3	−5.2	1.9
W02	3	1.63E–01	2.05E–02	222	67	−118	27.6	−44.1	−28.3	1.8
X01	4	3.03E–01	3.04E–02	57	79	−37	20.4	68.5	−11.1	2.0
X02	4	1.67E–01	3.00E–02	173	89	152	14.9	47.2	37.9	2.7
X03	4	2.84E–01	6.81E–02	149	86	−144	28.9	−64.4	6.7	1.3
X04	4	4.77E–01	3.23E–02	265	81	−87	42.5	−5.3	−52.2	1.7
Y01	4	3.21E–01	2.95E–02	95	64	31	93.2	−1.5	5.3	2.4

The highlighted events are classified as events with reliably determined moment tensors. The ratio min/max denotes the ratio of the minimum to maximum eigenvalues of the inverted system matrix (see Zahradník et al., 2008a).

Table 6
Non-DC components.

Method	Number of events	Mean DC [%]	Mean CLVD [%]	Mean ISO [%]	Mean |CLVD| [%]	Mean |ISO| [%]	Correlation CLVD-ISO	Ratio vP/vS
AMT	14	61.4	13.9	7.4	21.9	16.7	0.74	1.46
Isola	15	59.7	−5.4	3.3	24.1	16.2	0.48	1.57

The v_P/v_S ratio is calculated according to Vavryčuk (2001, Eq. (17)).

Table 7
Inversion for stress.

Method	Number of events	Az_1 [°]	Pl_1 [°]	Az_2 [°]	Pl_2 [°]	Az_3 [°]	Pl_3 [°]	Shape ratio
Focmec	16	220	25	72	61	316	14	0.60
AMT	14	210	25	78	55	311	23	0.61
Isola	15	215	5	107	74	306	15	0.44

Az_1, Pl_1, Az_2, Pl_2, Az_3, and Pl_3 are the azimuths and plunges of the principal stress directions σ_1, σ_2 and σ_3, respectively.

Heidbach, O., Tingay, M., Barth, A., Reinecker, J., Kurfeß, D., Müller, B., 2008. The World Stress Map database release 2008. doi:10.1594/GFZ.WSM.Rel2008.
Herrmann, R.B., 1979. FASTHYPO — a hypocenter location program. Earthquake Notes 50 (2), 25–37.
Hók, J., Bielik, M., Vanko, J., Kováč, P., Šujan, M., 2000. Neotectonic character of Slovakia (in Slovak with English summary). Mineralia Slovaca 32, 459–470.
Jarosinski, M., 1998. Contemporary stress field distortion in the Polish part of the western outer Carpathians and their basement. Tectonophysics 297 (1–4), 91–119.
Jarosinski, M., 2005. Ongoing tectonic reactivation of the Outer Carpathians and its impact on the foreland: Results of borehole breakout measurements in Poland. Tectonophysics 410, 189–216.
Julian, B.R., Miller, A.D., Foulger, G.R., 1998. Non-double-couple earthquakes 1. Theory. Rev. Geophys. 36, 525–549.
Kárník, V., 1968. Seismicity of the European Area. Part 1. Academia, Praha.
Kikuchi, M., Kanamori, H., 1991. Inversion of complex body waves—III. Bull. Seismol. Soc. Am. 81, 2335–2350.
Kováč, M., Bielik, M., Hók, J., Kováč, P., Kronome1, B., Labák, P., Moczo, P., Plašienka, D., Šefara, J., Šujan, M., 2002. Seismic activity and neotectonic evolution of the Western Carpathians (Slovakia). EGU Stephan Mueller Special Publication Series 3, pp. 167–184.
Lay, T., Wallace, T.C., 1995. Modern Global Seismology. Academic Press, N.Y.
Lenhardt, W.A., Švancara, J., Melichar, P., Pazdírková, J., Havíř, J., Sýkorová, Z., 2007. Seismic activity of the Alpine–Carpathian–Bohemian Massif region with regard to geological and potential field data. Geol. Carpath. 58 (4), 397–412.
Marko, F., Fodor, L., Kováč, M., 1991. Miocene strike-slip faulting and block rotation in Brezovské Karpaty Mts. (Western Carpathians). Mineralia Slovaca 23, 189–200.
Miller, A.D., Foulger, G.R., Julian, B.R., 1998. Non-double-couple earthquakes 2: Observations. Rev. Geophys. 36, 551–568.
Müller, B., Zoback, M.L., Fuchs, K., Mastin, L., Gregersen, S., Pavoni, N., Stephansson, O., Ljunggren, C., 1992. Regional patterns of tectonic stress in Europe. J. Geophys. Res. 97, 11.783–11.803.
Nemčok, M., Marko, F., Kováč, M., Fodor, L., 1989. Neogene tectonics and paleostress changes in the Czechoslovakian part of the Vienna Basin. Geol. B.-A. 132, 443–458.
Reinecker, J., 2000. Stress and deformation: Miocene to Present-day tectonics in the Eastern Alps. Tübinger Geowissenschaftliche Arbeiten, Reihe A, 55, p. 128.
Réthly, A., 1907. Earthquakes in Hungary in 1906 (in Hungarian) M. Kir. Orsz. Meteorológiai és Földmágnességi Intézet. Budapest.

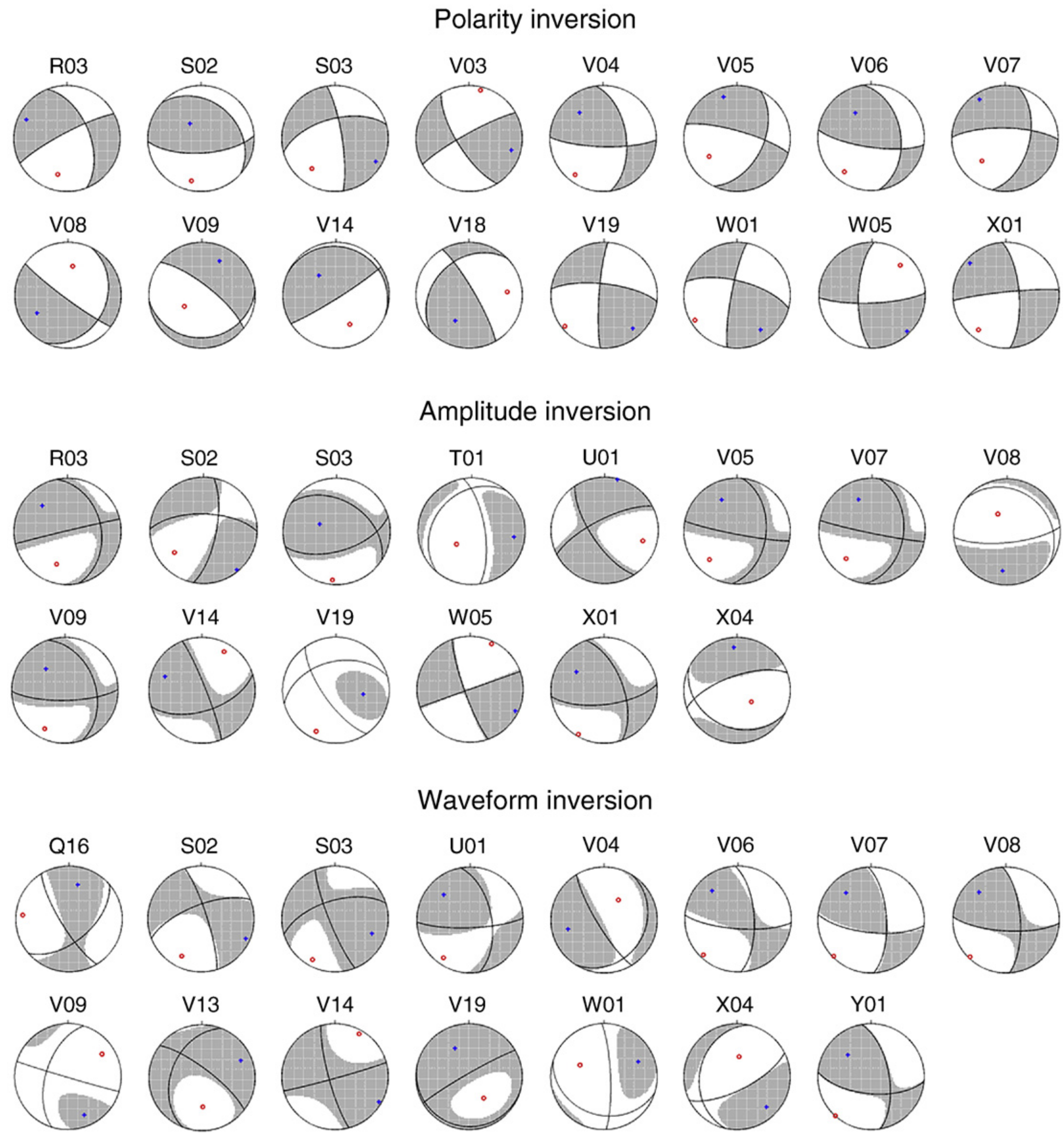

Fig. 13. Reliably determined focal mechanisms calculated using polarities of P waves, amplitudes of P waves and complete waveforms. The lower-hemisphere equal-area projection is used.

Šefara, J., Kováč, M., Plašienka, D., Šujan, M., 1998. Seismogenic zones in the Eastern Alpine – Western Carpathian – Pannonian junction area. Geol. Carpath. 49 (4), 247–260.

Šílený, J., 2009. Resolution of non-double-couple mechanisms: Simulation of hypocenter mislocation and velocity structure mismodeling. Bull. Seismol. Soc. Am. 99 (4), 2265–2272. doi:10.1785/0120080335.

Šílený, J., Vavryčuk, V., 2002. Can unbiased source be retrieved from anisotropic waveforms by using an isotropic model of the medium? Tectonophysics 356, 125–138. doi:10.1016/S0040-1951(02)00380-3.

Snoke, J.A., 2003. FOCMEC: FOcal MEChanism determinations. In: Lee, W.H.K., Kanamori, H., Jennings, P.C., Kisslinger, C. (Eds.), International Handbook of Earthquake and Engineering Seismology. Academic Press, San Diego. Chapter 85.12.

Sokos, E., Zahradník, J., 2009. ISOLA — A Fortran code and Matlab GUI to perform multiple-point source inversion of seismic data. Comput. Geosci. 34, 967–977.

Stammler, K., 1993. Seismic-Handler — Programmable multichannel data handler for interactive and automatic processing of seismological analyses. Comput. Geosci. 19 (2), 135–140.

Vavryčuk, V., 2001. Inversion for parameters of tensile earthquakes. J. Geophys. Res. 106 (B8), 16.339–16.355. doi:10.1029/2001JB000372.

Vavryčuk, V., 2005. Focal mechanisms in anisotropic media. Geophys. J. Int. 161, 334–346. doi:10.1111/j.1365-246X.2005.02585.x.

Vavryčuk, V., 2009. The Amplitude Moment Tensor Inversion — program AMT. Computer codes library, Institute of Geophysics, Prague.

Vavryčuk, V., Bohnhoff, M., Jechumtálová, Z., Kolář, P., Šílený, J., 2008. Non-double-couple mechanisms of micro-earthquakes induced during the 2000 injection experiment at the KTB site, Germany: A result of tensile faulting or anisotropy of a rock? Tectonophysics 456, 74–93. doi:10.1016/j.tecto.2007.08.019.

Zahradník, J., Serpetsidaki, A., Sokos, E., Tselentis, G.-A., 2005. Iterative deconvolution of regional waveforms and double-event interpretation of the 2003 Lefkada earthquake, Greece. Bull. Seismol. Soc. Am. 95, 159–172.

Zahradník, J., Janský, J., Plicka, V., 2008a. Detailed waveform inversion for moment tensors of M 4 events: Examples from the Corinth Gulf, Greece. Bull. Seismol. Soc. Am. 98 (6), 2756–2771. doi:10.1785/0120080124.

Zahradník, J., Sokos, E., Tselentis, G.-A., Martakis, N., 2008b. Nondouble-couple mechanism of moderate earthquakes near Zakynthos, Greece, April 2006; explanation in terms of complexity. Geophys. Prospect. 56, 341–356.

Zsíros, T., 2005. Seismicity of the Western-Carpathians. Acta Geodaet. Geophys. Hungaria 40 (3–4), 455–467.

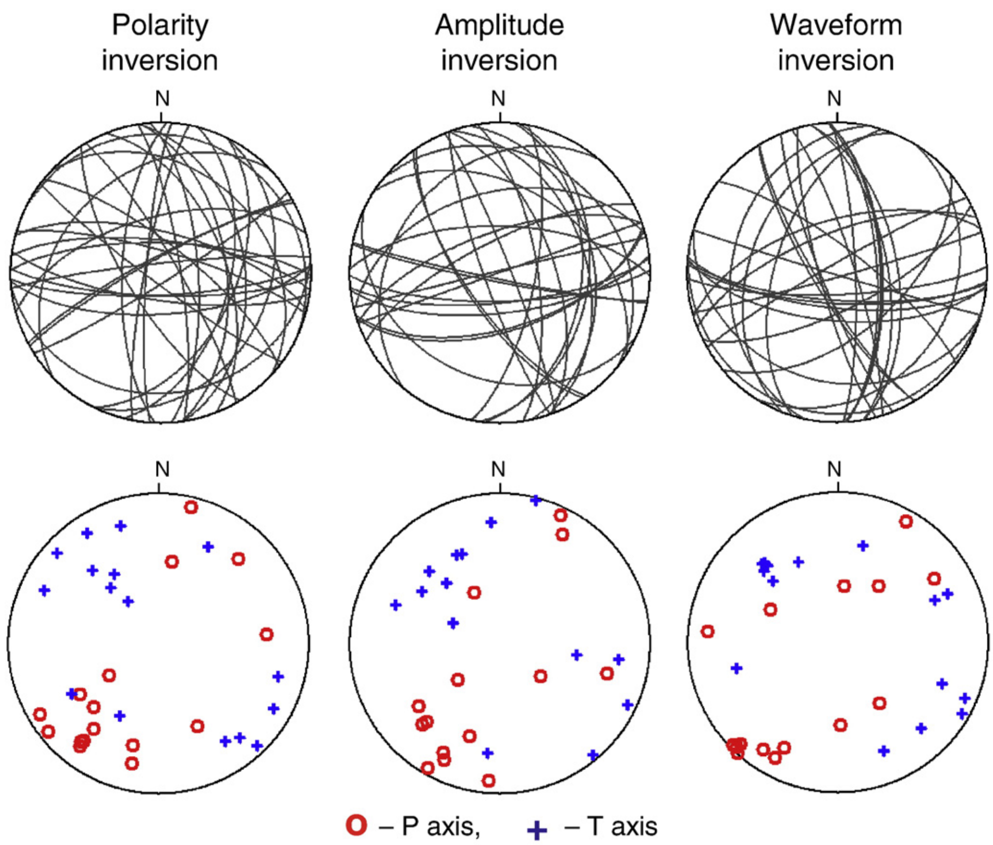

Fig. 14. Nodal lines and P/T axes of: 16 reliable focal mechanisms determined from the P-wave polarities (left-hand plots), 14 reliable moment tensors determined from P-wave amplitudes (middle plots), and 15 reliable moment tensors determined from complete waveforms (right-hand plots). The lower-hemisphere equal-area projection is used.

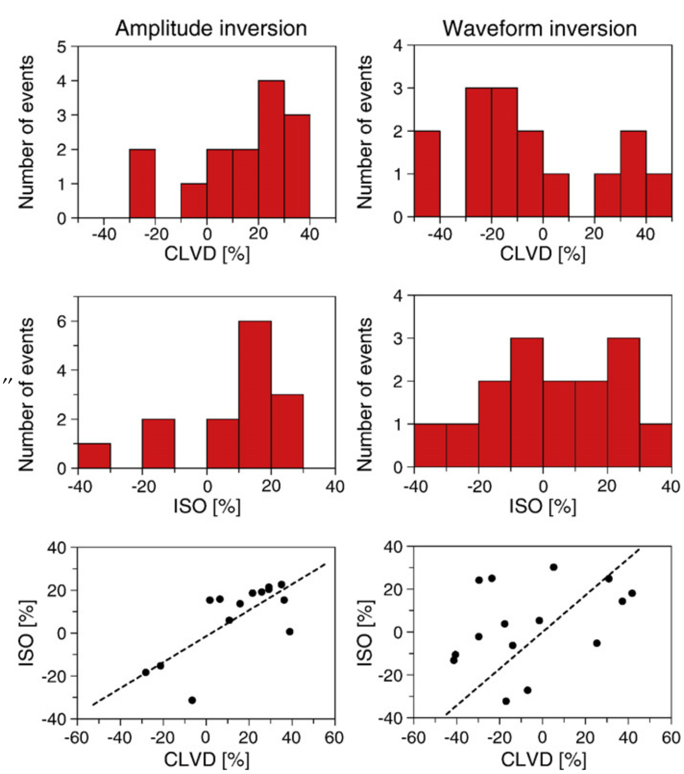

Fig. 15. Non-DC components of the moment tensors calculated using the amplitude (left-hand plots) and waveform (right-hand plots) inversions. Upper plots — histograms of the CLVD component, middle plots — histograms of the ISO component, and lower plots — the ISO component versus the CLVD component. The dashed line shows the linear regression between the ISO and CLVD.

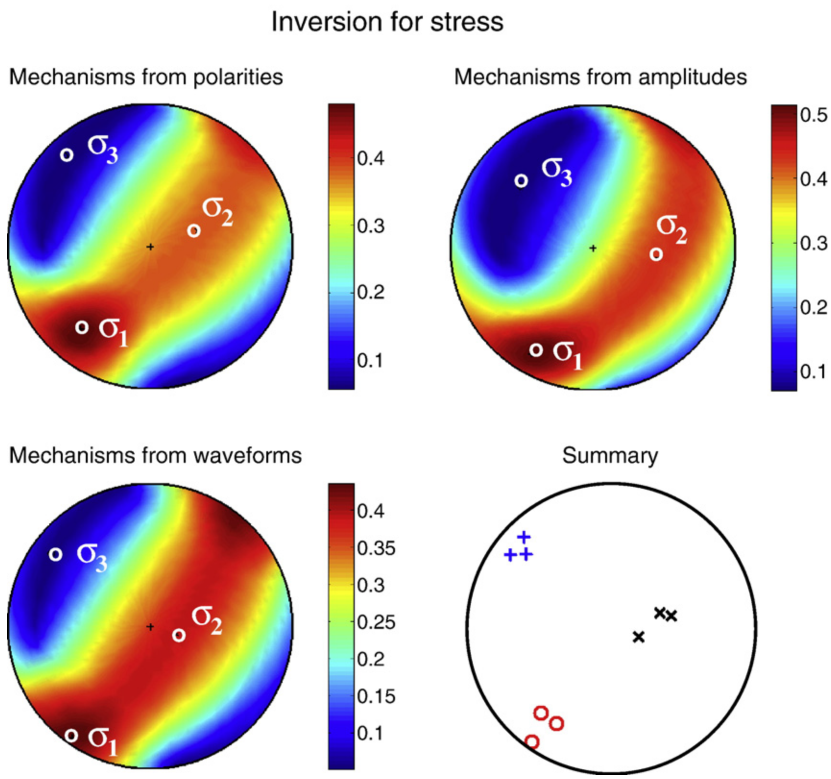

Fig. 16. The inversion for stress using the Angelier (2002) method. Stress is inverted using the focal mechanisms calculated from: the P-wave polarities (Focmec), the P-wave amplitudes (AMT), and the complete waveforms (Isola). The lower right-hand plot summarizes the results of the three inversions. The colour scale indicates the value of the SSSC fit for the direction of the maximum compression (principal stress σ_1). The optimum position of the maximum compression is at the maximum of the SSSC fit. The directions of the principal stresses in the lower right-hand plot are marked by red circles for σ_1, by black crosses for σ_2, and by blue plus signs for σ_3.

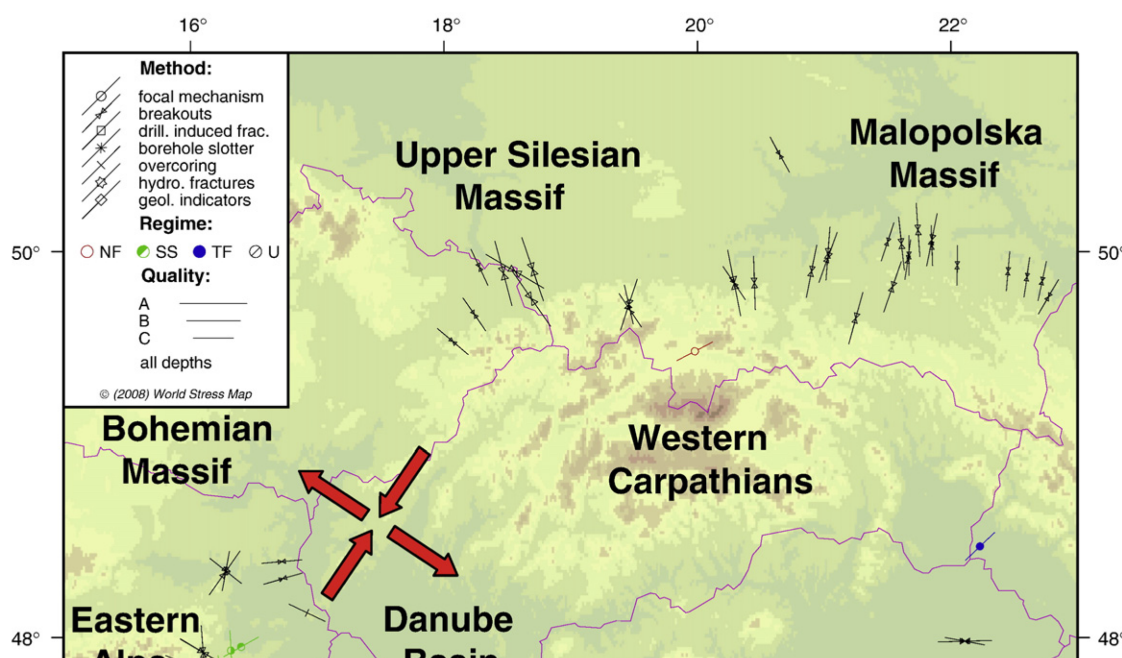

Fig. 17. Stress map in the Western Carpathians region and adjacent areas. Red arrows show the retrieved direction of the maximum compression and the maximum extension in the Dobrá Voda area. The other stress measurements are taken from the World Stress Map site (Heidbach et al., 2008).